1-1-2014

Near- and far-field measurements of phase-ramped frequency selective surfaces at infrared wavelengths

Eric Tucker

Jeffrey D'Archangel
University of Central Florida

Markus B. Raschke

Glenn Boreman

Recommended Citation

Near- and far-field measurements of phase-ramped frequency selective surfaces at infrared wavelengths

Eric Tucker, Jeffrey D'Archangel, Markus B. Raschke, and Glenn Boreman

View Online   Export Citation   CrossMark

ARTICLES YOU MAY BE INTERESTED IN

Near- and far-field measurements of phase-ramped frequency selective surfaces at infrared wavelengths

Eric Tucker,[1] Jeffrey D'Archangel,[2] Markus B. Raschke,[3] and Glenn Boreman[1,a)]

[1]*Department of Physics and Optical Science, University of North Carolina at Charlotte, 9201 University City Blvd., Charlotte, North Carolina 28223, USA*
[2]*CREOL, The College of Optics and Photonics, University of Central Florida, 4304 Scorpius St., Orlando, Florida 32816, USA*
[3]*Department of Physics, Department of Chemistry, and JILA, University of Colorado, 390 UCB, Boulder, Colorado 80309, USA*

Near- and far-field measurements of phase-ramped loop and patch structures are presented and compared to simulations. The far-field deflection measurements show that the phase-ramped structures can deflect a beam away from specular reflection, consistent with simulations. Scattering scanning near-field optical microscopy of the elements comprising the phase ramped structures reveals part of the underlying near-field phase contribution that dictates the far-field deflection, which correlates with the far-field phase behavior that was expected. These measurements provide insight into the resonances, coupling, and spatial phase variation among phase-ramped frequency selective surface (FSS) elements, which are important for the performance of FSS reflectarrays. [http://dx.doi.org/10.1063/1.4890868]

I. INTRODUCTION

Frequency selective surfaces (FSS) can be employed to tune surface properties including absorptivity, reflectivity, and transmission.[1,2] These properties are mostly dependent on the size and geometry of the conductive FSS elements, but are also affected by the dielectric optical properties of the material of the elements, the composition of the substrate/dielectric layer, and the spatial arrangement of these elements.[1] FSS have uses as filters, polarizers, thermal emitters, and other applications.[1,2] One application of particularly great interest is wave front shaping for beam deflection and focusing.

Through purposely varying the resonant frequency of the FSS elements, the phase shift upon reflection of an incident beam of a given wavelength can be tuned, which follows the Kramers-Kronig relation as applies to electromagnetic resonance and reflected phase. This idea has been scaled from RF to infrared wavelengths where arrays of metal patch elements showed varying phase changes upon reflection when the size of the patches was adjusted.[3] Even though these different size structures were not arranged in such a way as to allow for wave front shaping, it still offered a proof-of-concept for the feasibility of using such elements at infrared wavelengths for this purpose.

Later, this concept was utilized through the arrangements of single and different size patch elements to allow for wave front shaping to focus a beam at infrared wavelengths.[4,5] For instance, in one case, it was demonstrated that single size patch elements could be arranged in concentric circular zones over a ground plane, which results in 180° phase steps and beam focusing in the infrared.

Also, FSS elements have been arranged as phase-ramped structures to allow for wave front shaping of a beam to deflect it away from the angle for specular reflection. In these phase-ramped frequency selective surfaces, FSS elements are arranged in a repeating unit cell of several elements in a row having a gradient of size, which results in a variation of the reflected phase across the surface. This has been successfully demonstrated in the terahertz and visible regions of the electromagnetic spectrum where a relatively high percentage of the incident beam was deflected at a specific angle.[6–8] For example, phase-ramped structures optimized for terahertz frequencies have been constructed from gold patch elements of different sizes arranged in repeating rows of six elements from smallest to largest.[6,8] Each of the elements was designed to initiate a different phase shift of the incident beam upon reflection and when combined in an array would steer a beam away from the specular reflection direction. It was found that the incident beam could be deflected at an angle off specular reflection, but that the resulting angle was relatively sensitive to fabrication imperfections, which limited how closely it matched the simulated value for this angle.

Even though the properties of interest for these phase-ramped structures are relatively straightforward to be measured in the far-field, the effective far-field response is determined by the near-field polarization, in particular, the spatial variation of the local optical phase that determines the far-field response. Scattering-type scanning near-field optical microscopy (*s*-SNOM) has proved particularly powerful in measuring both the amplitude and phase of the electric near-field distribution on antenna, plasmonic, and metamaterial structures.[9–20] Previously, we investigated phase-ramped end-loaded cross structures with *s*-SNOM.[21] However, to our knowledge, no further efforts have yet been

---

a)Author to whom correspondence should be addressed. Electronic mail: gboreman@uncc.edu.

made to explore the near-field response of other types of phase-ramped structures in the mid-infrared. In particular, there is very little work comparing the near- and far-field phase for these types of structures.[22]

Here, we measure and simulate the near- and far-field response of phase-ramped loop and patch structures when illuminated with mid-infrared radiation. Measurements of the phase shift and coupling in the near-field response of square loop and patch elements arranged in a gradient of size were compared to simulations of the phase shift in the near- and far-field. Measurements of the beam deflection were made when the structures were illuminated normal to the surface plane and compared to simulations of the beam deflection. We found that the phase-ramped structures deflected a beam away from specular reflection and were able to measure much of the near-field phase that dictates the far-field phase behavior of these structures.

II. MATERIALS AND METHODS

The phase-ramped structures were fabricated in a similar manner as outlined previously and a schematic of a representative local unit-cell of one size structure in the repeating phase-ramped pattern is shown in Fig. 1(a).[21,23] The patterns consist of arrays of loops or patches of the dimensions labeled in Fig. 1(a) that were arranged in a repeating arrangement of five elements of different sizes aligned in a row. Briefly, these samples were fabricated by thermally depositing an optically thick aluminum ground plane having a thickness of 150 nm on a silicon wafer. Then, a benzo-cyclobutene (BCB) (Dow Cyclotene 3022–35 resin) dielectric standoff layer of 1.2 μm thickness (h) was deposited by spin coating the material on the sample and curing in a nitrogen environment. This material is easier to deposit compared to thermally evaporated standoff layers and still has relatively low loss over a wide spectral range in the mid-infrared. Electron beam lithography was used to define the phase-ramped structures, which was followed by development of the resist, metallization, and lift-off. The resulting structures are shown in the scanning electron micrographs in Figs. 1(b) and 1(c). The Al elements had a height (t) of 75 nm and periodicity of 5 μm. The phase-ramped loop array consisted of element sizes of a = 1.25,

1.625, 2.000, 2.375, and 2.750 μm while the phase-ramped patch array consisted of element sizes of a = 1.625, 2.000, 2.375, 2.750, and 3.125 μm.

Near-field simulations were performed with Comsol Multiphysics and far-field simulations were performed with Ansoft HFSS. In many cases, the simulations were performed with both software packages to check for consistency of the result. Frequency-dependent optical constants of the materials, obtained by variable-angle spectroscopic ellipsometry, were employed in the numerical simulations. In all cases, the incident wave is simulated with polarization consistent with how the measurements were performed. In the near-field simulations, the amplitude and phase of E_z was evaluated 25 nm above the structures.

Measurements of the deflection angle relative to specular reflection were performed by illuminating the phase-ramped patches and loops from normal to the surface plane with 10.6 μm radiation (L4S, Access Laser Company). An iris was used to aperture the beam to roughly the size of the arrays being measured. A thermal infrared detector mounted on a rotatable arm extending ~0.25 m away from the structures was used to measure the power at all angles of deflection. All reported values were converted to realized gain, which was based on an additional measurement where just the incident beam power was determined.

Near-field measurements were made with a custom-built *s*-SNOM that is similar to the instrument that has been described previously.[21,23,24] A schematic showing the experimental layout is shown in Fig. 2. This instrument employs an atomic force microscope (AFM), which was modified to allow for sample scanning (Innova, Bruker). Platinum-Iridium coated tips are used, which had a resonant oscillation frequency of 240–280 kHz (Arrow-NCPt, Nanoworld). Mid-IR radiation for the near-field measurements is provided by a CO_2 laser.

In the configuration for the *s*-SNOM measurement, part of the radiation from the CO_2 laser is reflected off a beam splitter (BS) towards the sample, while a comparable fraction of the remaining radiation is transmitted through the beam splitter towards a reference mirror (RM). The s-polarized
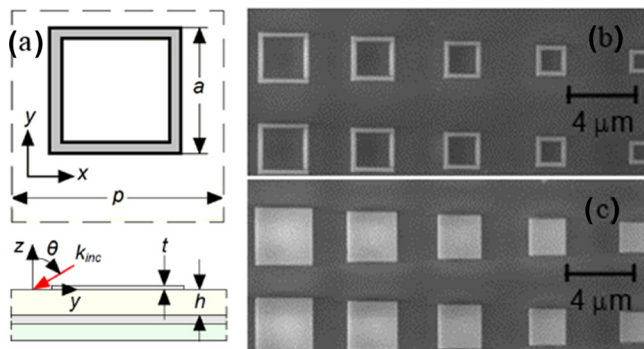

FIG. 1. (a) Schematic showing the sample design of the phase-ramped structures. Here, a single loop element is drawn as an example. SEM micrographs of the (b) phase-ramped looped structures and (c) phase-ramped patch structures.
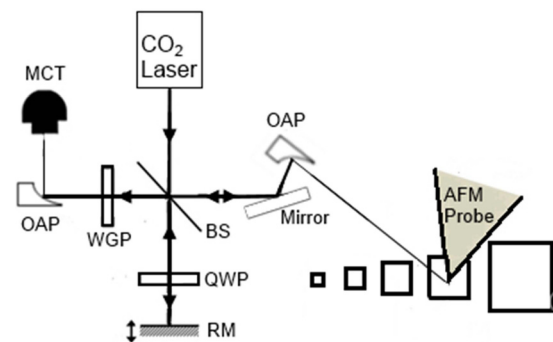
FIG. 2. Schematic showing the configuration used for the *s*-SNOM measurement where OAP reflectors have been incorporated for focusing at the sample as well as at the MCT detector. Cross-polarized excitation and detection is implemented through the use of wire grid polarizers (WGP). Part of the incident radiation for the CO_2 laser is transmitted through a BS into a reference path constituting a piezo driven RM and quarter wave plate (QWP), which allows for amplitude and phase measurement of the near-field signal.

radiation is directed towards an off-axis parabolic reflector (OAP), which reflects the radiation at 60° with respect to the surface normal and focuses the beam to an approximately 60 μm size spot on the sample. The AFM is operated in tapping mode and the tip scatters the near-field into detectable far-field radiation. This scattered radiation emanating from the tip is collected using the same optics for the incident beam and is detected interferometrically with the mercury-cadmium-telluride (MCT) detector.[25,26] Polarization selective optics allow for predominantly p-polarized radiation to reach the detector, which restricts the measurement to mainly the E_z field.[25] AFM height images are collected simultaneously with the s-SNOM signal (S_d), which is proportional to

$$S_d \propto I = |E_{scat} + E_{ref}|^2 + I_b$$
$$= |E_{scat}|^2 + |E_{ref}|^2 + 2|E_{scat} \times E_{ref}| \cos\phi + I_b, \quad (1)$$

where ϕ represents the phase difference between the reference and scattered beam, E_{scat} is the electric field of the scattered beam, and E_{ref} is the electric field of the reference beam. In addition, I_b is background radiation originating from stray reflections and scattering from the AFM probe and sample surface, which does not contain information associated with the near-field signal.[27–30] A lock-in amplifier, which demodulates the signal from the detector at the 2nd harmonic of the tip dither frequency, is used to discriminate much of the scattered near-field signal from background. Images are collected at different positions of the RM (corresponding to different reference phases) to allow for determination of amplitude and phase of the near-field signal. Specifically, this is accomplished by performing least-squares, point-by-point fits with a cosine function to the set of phase images.[21] Line scan analysis of phase and AFM height measurements was performed using WSxM version 3.1.[29]

III. RESULTS

Simulations were performed to determine the relative phase change upon reflection and absorption when uniform arrays of different size loop and patch elements are illuminated with 10.6 μm wavelength radiation. More specifically, periodic boundary conditions were used to define an infinite, repeating unit cell of one size loop or patch array. Then, a parametric sweep was performed where the magnitude and phase of the reflection coefficient was determined for this uniform, infinite array as a function of the size of the structure. Specifically, the thickness of the BCB and elements is equal to the values from the fabricated phase-ramped structures while the length (a) of the elements is varied and the width is kept equal to the length.

First, the simulation was performed with the incident wave having an angle of incidence equal to 60° off-normal, which corresponds to the same conditions for the near-field measurements. The magnitude and phase of the reflection coefficient was solved as a function of the size of the structures. Fig. 3(a) shows the relative phase of the reflected incident wave and the corresponding absorptance as a function of size of a loop element. Similarly, Fig. 3(b) shows relative phase of the reflected incident wave and absorptance versus the size of a patch element. In both plots (Figs. 3(a) and 3(b)), black, square points along the curves for the reflected phase correspond to the sizes of the loops and patches in the phase-ramped structures that were fabricated.

Figs. 3(a) and 3(b) show that both elements have a fundamental and harmonic mode when illuminated at 60° off-normal with 10.6 μm wavelength radiation, with only the fundamental mode of high absorptance covered by the fabricated loops and patches. Fig. 3(a) is similar to a plot in a previous article except reflected phase is included here.[23] The higher absorptance has been shown previously to be primarily due to the lower conductivity of metals at infrared wavelengths, especially aluminum, compared to at much lower frequencies where the conductivity of metals are much greater.[31,32] Also, the absorptance can be affected by the thickness of the dielectric layer.[4,8] However, except for the middle size structure, all the remaining structures are detuned from resonance. So, overall we expect that the actual fabricated phase-ramped structures should show relatively low absorptance despite the relatively high absorptance at the fundamental mode, which is important for the performance as a reflectarray. In addition, in Fig. 3, both curves for the phase of reflected incident wave show that the maximum possible range for the reflected phase is only slightly less than 360°. Previously, it was shown that this value is diminished by lower conductivities of the metal used as the FSS element, high loss tangent of the dielectric layer, or larger thicknesses of the dielectric layer, but phase ranges similar to this value have yielded good results as a reflectarray.[4,8,31,33] Also critical to the performance of a reflectarray of constant periodicity is the need to have a relative constant progressive phase change of the reflected incident beam between each size structure.[7,8,34] As shown in both plots in

FIG. 3. Graphs showing simulated reflected phase (red solid line) and absorptance (blue dashed line) versus (a) loop and (b) patch size when the structures were illuminated at 60° off-normal with a 10.6 μm wavelength incident wave. Black, square points represent the dimensions corresponding to the fabricated structures in Fig. 1.
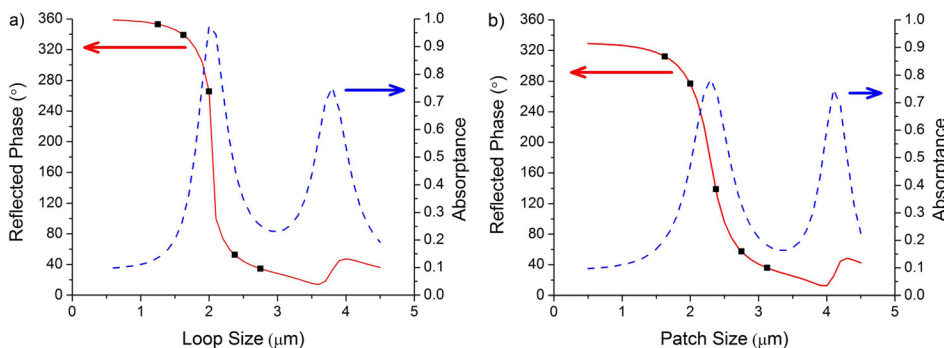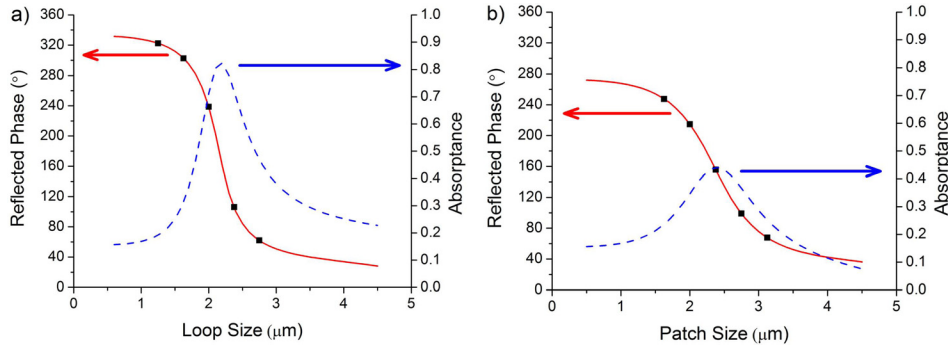
FIG. 4. Graphs showing simulated reflected phase (red solid line) and absorptance (blue dashed line) versus (a) loop and (b) patch size when the structures were illuminated with a 10.6 μm wavelength incident wave normal to the surface plane. Black, square points represent the dimensions corresponding to the fabricated structures in Fig. 1.

Figs. 3(a) and 3(b), the fabricated phased-ramped structures have a variable progressive phase change among neighboring elements in size between the structures when illuminated from 60° off-normal (black, square points).

Similar parametric simulations were performed in HFSS where arrays of different size Al loop and patch elements were illuminated with an incident wave with a wavelength of 10.6 μm normal to the surface plane, which is shown in Figs. 4(a) and 4(b). Similar to the above, there is a relatively high absorptance at the fundamental mode for both phase-ramped structures, so the center structure should show relatively strong absorptance. Again, due to the remaining size structures being all detuned from resonance, we expect the overall absorptance to be much lower. As with Figs. 3(a) and 3(b), both plots have a maximum range for the phase of the reflected incident wave that is only slightly less than 360°. However, the progressive phase change between the different size elements is relatively constant and shows significantly less variation compared to Figs. 3(a) and 3(b), especially for the phase-ramped patches. These results suggest that the phase-ramped structures should show a relatively good performance at this angle of incidence.

Since the simulations where uniform arrays of loops and patches are illuminated at normal incidence suggest that the phase-ramped loops and patch structures should show relatively good beam steering performance (Figs. 4(a) and 4(b)), measurements of this deflection angle were done under these conditions. As demonstrated previously, the local phase shift of the beam in a reflectarray is caused by the differences in phase upon reflection from the elements instead of through optical path differences, which is the main principal of operation for an optical grating.[7,35] So, most conveniently, the previously derived equation describing the operation of reflectarrays can be rearranged to relate the reflected phase by each element to the predicted deflection angle (θ) according to

$$\phi_n = \frac{2\pi n p}{\lambda_0} \times \sin(\theta) + \phi_0, \qquad (2)$$

where λ_0 is the free space wavelength, p is the periodicity for the element spacing, n refers to the nth element in the phase ramp, ϕ_0 is the reflected phase from the first element, and ϕ_n is the reflected phase from the nth element.[7,8] The previous equation can be rewritten and rearranged in order to solve for the deflected angle, which results in the following:

$$\sin(\theta) = \frac{\Delta\phi\lambda_0}{2\pi p}, \qquad (3)$$

where $\Delta\phi$ is the progressive phase change. This equation was used to calculate the relative angle these structures should steer a 10.6 μm beam away from the angle of specular reflection or, in this case, away from normal to the surface plane. The phase change between different size elements had a small amount of variability, so the average phase change was employed in the above equation. The results of this calculation show that the phase-ramped loops and patches should both steer a beam approximately 25° away from the angle for specular reflection.

Far-field measurements of this deflection angle were performed and are shown as polar plots of realized gain in Fig. 5 where realized gain is defined as the ratio of the radiated power in each direction to the power of the incident beam. For the phase-ramped loops, the measured deflected angle is 23° while the phase-ramped patches have a deflected angle of 24°, which is relatively close to the calculated values of 25° for both structures. One difference between the calculated and measured beam deflection angle is that the calculation is based on values of reflected phase obtained from simulations of uniform arrays of elements while the measurement is of the phase-ramped structures having different size elements. More specifically, the simulations of the uniform arrays have adjacent unit cells with structures equal in size while the measurement is of the phase-ramped structure having adjacent unit cells of different sizes, which are expected to have different coupling among the neighboring elements.[6,8] Previous articles have shown that differences in
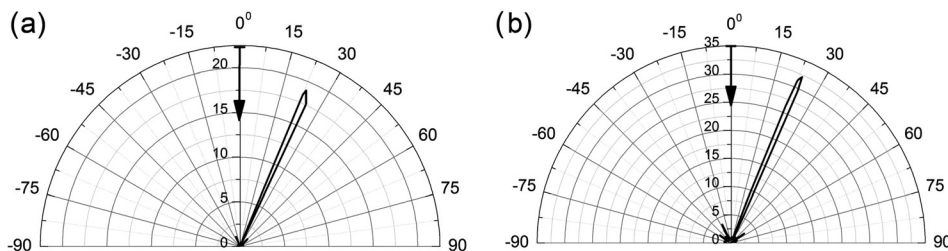

FIG. 5. Polar plots showing measured realized gain values as a function of angle when the phase-ramped loops (a) and patches (b) were illuminated normal to the surface plane. Realized gain is calculated from the ratio of the radiated power in each direction to power of the incident beam. The arrow indicates the direction of illumination.
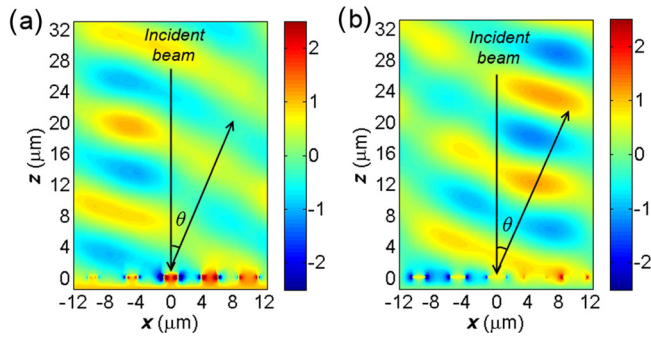
FIG. 6. Surface plots of simulated instantaneous scattered field in the x-direction (E_x) resulting from illumination of the phase-ramped loops (a) and patches (b) normal to the surface plane. The phase-ramped structures are located at the bottom of the figure with the smallest structure towards the bottom left. The arrows indicate the direction of illumination and deflection as a guide to the eye.

coupling between the elements strongly affects the wave front of the deflected beam in similar phase-ramped structures designed for other wavelengths, which should affect the angle for the deflected beam.[6]

Therefore, additional simulations were performed where the beam deflection is determined more directly and the

deflected wave front can be visualized. Similar to the experiment, in separate simulations, a plane wave normal to the surface plane is directed towards the repeating, infinite phase-ramped loop and patch structure. Figs. 6(a) and 6(b) show the resulting instantaneous scattered E-field (in the x direction) along the xz plane above the structures. This simulation shows that the wave front of the deflected beam is approximately planar and that the angle for deflection is nearly identical to those found in the measurements. Any further differences between the measured and simulated deflected angles can likely be attributed to fabrication imperfections. For instance, it has been shown previously that the beam deflection angle is sensitive to the dielectric layer thickness.[8] The simulated results of the deflected angle are based on a thickness for the dielectric layer that was a target for the fabrication, but it is likely that the actual thickness for this layer deviates from this value to some extent.

Next, measurements were performed of the near-field distribution of the phase-ramped structures. More specifically, it was of interest to gain insight into how the relative phase upon reflection that is observed in the far-field compares to the relative phase observed in the near-field. In addition, it is of interest to observe how fabrication tolerances
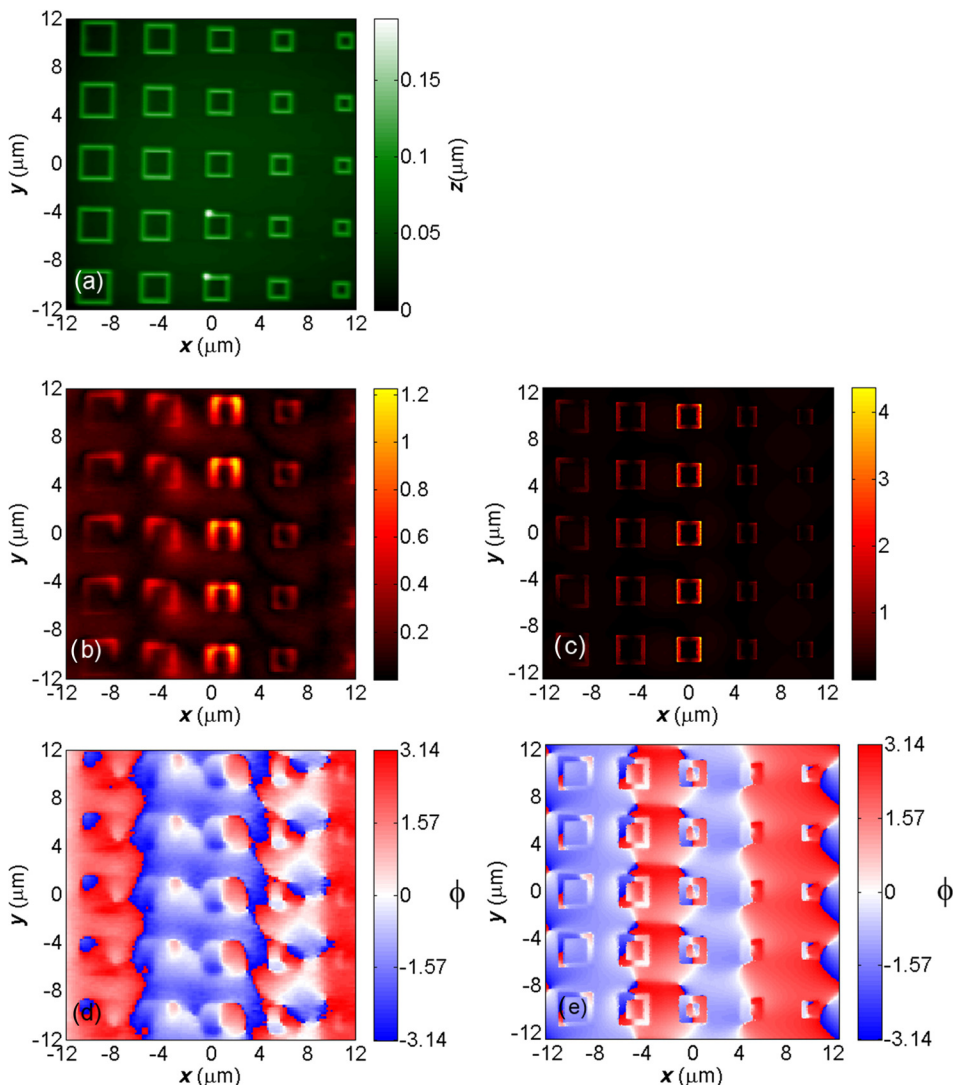

FIG. 7. AFM topography (a) and measured ((b) and (d)) and simulated ((c) and (e)) near-field images for the phase-ramped loop structure with (b) measured *s*-SNOM amplitude, (c) simulated amplitude, (d) measured *s*-SNOM phase, and (e) simulated phase. In the measured and simulated amplitude images, the values for the z-axis are proportional to E_z.
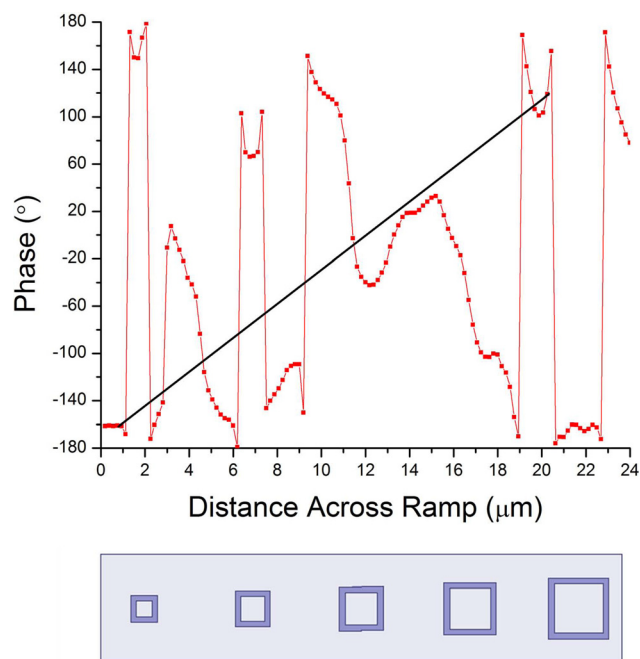
FIG. 8. Line scan analysis of phase across the middle of the image shown in Fig. 7(d) versus distance across the image in the x direction. When considering phase values in areas corresponding to the location of the loop elements, there is a ∼270° phase range across the unit cell. The black line is present as a guide to the eye.

affect the near-field phase response, especially differences in the simulated and experimental near-field phase. Previously, fabrication tolerances showed pronounced effects on the far-field phase response near resonance for metallic structures due to the higher phase variation with elements around this resonant size.[8] These observations should yield useful insight into future designs for optimizing the phase upon reflection that the structures cover and minimizing the effect of coupling among elements.

First, near-field measurements were collected for the phase-ramped loop structure via s-SNOM. Figs. 7(a)–7(e) show AFM topography as well as near-field measurements and simulations for the phase-ramped looped structure. In the measured and simulated amplitude images in Figs. 7(b) and 7(c) one can see that the middle structure shows the strongest amplitude signal, which is consistent with the simulation in Fig. 3(a) where it was suggested that the middle structure was the most resonant. Also, the loops of smaller and larger size have much less amplitude signal compared to the middle structure, which is also consistent with the simulation in Fig. 3(a) where they are shown to have less absorptivity and are off-resonance. In Figs. 7(d) and 7(e), there is a qualitative match between the simulated and measured phase. Despite best efforts to synchronize the wrapping of the phase in both images, there are still slight differences between the measurement and simulation. These differences in the simulated and measured near-field phase can be attributed to the diminished field on the less resonant elements compared to the more resonant element, which increase errors in the phase data as has been seen previously.[36] In contrast, the phase in proximity to the more resonant element

where there is stronger field shows much greater consistency between the simulations and experimental data. In Figs. 7(d) and 7(e), one can still see that the phase images show that each size element is out of phase with the other sizes, although it is difficult to see the continuous phase gradient across the structures.

In order to more quantitatively examine the progressive near-field phase transition over the phase-ramped loops, a line scan analysis was performed of the measured phase across the different size loops. This was accomplished by plotting the phase data across the middle of Fig. 7(d) as a function of the distance across the image as shown in Fig. 8. When considering only phase values attributed to the loops, one can see that there is an approximate linear phase ramp across the elements. This is consistent with the linear relationship of the far-field phase versus distance across the surface shown in Eq. (2). Also, one can see that there is an approximately 270° phase range across the loops, which is less than the simulated far-field phase range shown in Fig. 3(a). However, this difference is expected as the ground plane and surrounding areas around the patch contribute a significant portion of the resulting phase shift observed in the far-field.[37,38] Also, as mentioned previously, the simulations in Fig. 3 were done using uniform arrays where adjacent unit cells contain structures equal in size while the measurement is of structures having different size neighboring elements, which is likely to contribute to the differences in the phase range values.

In addition, near-field measurements were collected by s-SNOM for the phase-ramped patch structure. Figs. 9(a)–9(e) show AFM topography as well as near-field measurements and simulations for the phase-ramped patch structure. As was observed for the phase-ramped loop structures, the measured and simulated amplitude images for the phase-ramped patch (Figs. 9(b) and 9(c)) show that the middle structure has the strongest amplitude signal. This is consistent with the simulation shown in Fig. 3(b) where it was suggested that the middle structure should indeed be the most resonant element. Also, the patches of smaller and larger size show a diminished amplitude signal compared to the resonant structure, which is also consistent with Fig. 3(b). In Figs. 9(d) and 9(e), it can be seen that the simulated and measured phase show a qualitative match where slight differences can again be attributed to the weaker field in some areas as shown by the amplitude image (Fig. 9(b)). Also, phase images for these structures show a variation in phase among the different size elements as was seen with the phase-ramped loop structures, which is also expected based on the graph shown in Fig. 3(b). As before, it is difficult to see the continuous phase gradient across the structures.

In order to more quantitatively examine the progressive near-field phase transition over the phase-ramped patches, a line scan analysis was performed of the measured phase across the different size structures. This was accomplished by plotting the phase data across the middle of Fig. 9(d) as a function of the distance across the image as shown in Fig. 10. As with the phase-ramped loop structure, when considering only phase values attributed to the patches, one can see
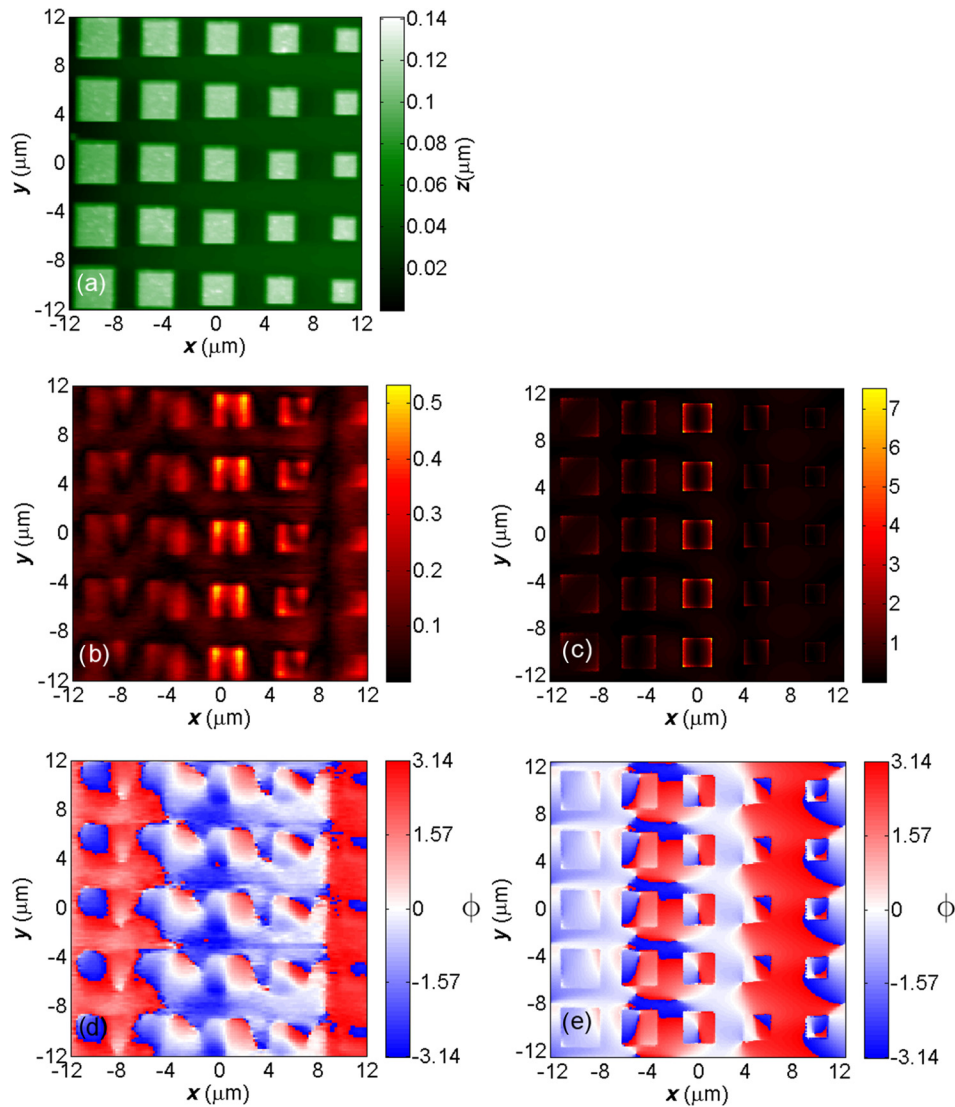
FIG. 9. AFM topography (a) and measured ((b) and (d) and simulated ((c) and (e)) near-field images for the phase-ramped patch structure with (b) measured s-SNOM amplitude, (c) simulated amplitude, (d) measured s-SNOM phase, and (e) simulated phase. In the measured and simulated amplitude images, the values for the z-axis are proportional to E_z.

that there is an approximate linear phase ramp across the elements, which is consistent with Eq. (2). Also, there is an approximately 300° phase range across these structures, which is less than the simulated far-field phase range observed in Fig. 3(b). As mentioned above, these values are expected to be different due to the ground plane and surrounding areas around the patches contributing to the phase observed in the far-field, but some of this difference could also be attributed to the simulation being comprised of a uniform array of elements while the experiment consists of non-uniform arrays of elements.

IV. CONCLUSION

We characterized phase-ramped loop and patch structures, which consist of loop and patch elements in periodic arrangements of five successive elements of different size to form square arrays of these elements. First, far-field simulations were performed on arrays of uniform elements to characterize the relative phase upon reflection and the absorptivity at 10.6 μm versus the size of the elements in the arrays. These results implied that both structures had potential to perform well as a reflectarray, especially at normal incidence. Results

from the far-field deflection measurements showed that the phase-ramped loops and patches deflected a 10.6 μm beam 23° and 24° away from normal to the surface plane, which were very close to calculated and simulated values for the angle of deflection. The experimental near-field results for both phase-ramped structures showed that the near-field phase showed the expected phase variation across the different size structures and qualitatively matched the simulated near-field phase. Line scan analysis of the near-field phase data for the phase-ramped loops and patches showed a linear relationship between near-field phase and the distance across the surface, consistent with Eq. (2). These results identify much of the near-field phase that dictates the far-field phase behavior of these phase ramp structures. The remaining contribution originates from the ground plane and surrounding areas around the elements, which was not able to be measured for these particular structures.

Despite the above results showing that these phase-ramped structures can perform well as a reflectarray in the mid-infrared, the performance could be improved further by changing the design to reduce absorptivity of these structures. This could be accomplished by using materials for the dielectric and FSS element that have less loss at the design
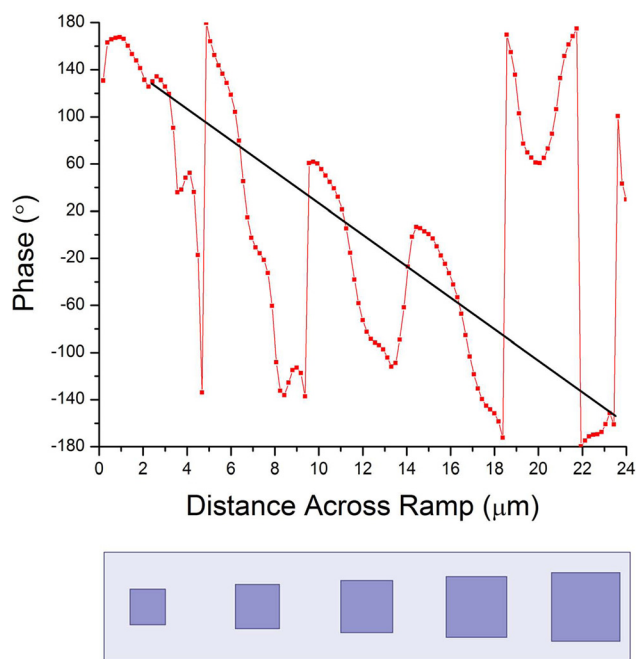
FIG. 10. Line scan analysis of phase across the middle of the image shown in Fig. 9(d) versus distance across the image in the x direction. When considering phase values in areas corresponding to the location of the patch elements, there is a ~300° phase range across the unit cell. The black line is present as a guide to the eye.

wavelength.[31] Also, it may be possible to reduce the absorptivity in this design by increasing the thickness of the dielectric layer, but it has been shown that a trade-off exist with the thickness of this layer regarding the range of the reflected phase and absorptance.[8] According to some articles, it has been suggested that, practically, a low-loss, high permittivity dielectric resonator antenna would yield better performance as a reflectarray for the infrared and visible frequencies.[7,31,39]

ACKNOWLEDGMENTS

[1]J. C. Vardaxoglou, *Frequency Selective Surfaces: Analysis and Design* (Research Studies Press, London, 1997), Vol. 997.
[2]R. Mittra, C. H. Chan, and T. Cwik, Proc. IEEE **76**, 1593 (1988).
[3]J. C. Ginn, B. A. Lail, and G. D. Boreman, IEEE Trans. Antennas Propag. **55**, 2989 (2007).
[4]J. Ginn, B. Lail, J. Alda, and G. Boreman, Opt. Lett. **33**, 779 (2008).
[5]J. Ginn, J. Alda, J. A. Gómez-Pedrero, and G. Boreman, Opt. Express **18**, 10931 (2010).
[6]T. Niu, W. Withayachumnankul, B. Ung, H. Menekse, M. Bhaskaran, S. Sriram, and C. Fumeaux, in *Proceedings of 37th International Conference on Infrared, Millimeter, and Terahertz Waves (IRMMW-THz)* (2012), p. 1.
[7]L. Zou, W. Withayachumnankul, C. Shah, A. Mitchell, M. Bhaskaran, S. Sriram, and C. Fumeaux, Opt. Express **21**, 1344 (2013).
[8]T. Niu, W. Withayachumnankul, B. Ung, H. Menekse, M. Bhaskaran, S. Sriram, and C. Fumeaux, Opt. Express **21**, 2875 (2013).
[9]S. Mastel, S. E. Grefe, G. B. Cross, A. Taber, S. Dhuey, S. Cabrini, P. J. Schuck, and Y. Abate, Appl. Phys. Lett. **101**, 131102 (2012).
[10]T. Zentgraf, J. Dorfmüller, C. Rockstuhl, C. Etrich, R. Vogelgesang, K. Kern, T. Pertsch, F. Lederer, and H. Giessen, Opt. Lett. **33**, 848 (2008).
[11]M. Schnell, P. Alonso Gonzalez, L. Arzubiaga, F. Casanova, L. E. Hueso, A. Chuvilin, and R. Hillenbrand, Nat. Photonics **5**, 283 (2011).
[12]R. Esteban, R. Vogelgesang, J. Dorfmüller, A. Dmitriev, C. Rockstuhl, C. Etrich, and K. Kern, Nano Lett. **8**, 3155 (2008).
[13]R. Vogelgesang, J. Dorfmüller, R. Esteban, R. T. Weitz, A. Dmitriev, and K. Kern, Phys. Status Solidi B **245**, 2255 (2008).
[14]J. Dorfmüüller, D. Dregely, M. Esslinger, W. Khunsin, R. Vogelgesang, K. Kern, and H. Giessen, Nano Lett. **11**, 2819 (2011).
[15]S. E. Grefe, D. Leiva, S. Mastel, S. D. Dhuey, S. Cabrini, P. J. Schuck, and Y. Abate, Phys. Chem. Chem. Phys. **15**, 18944 (2013).
[16]A. Apuzzo, M. Fevrier, R. Salas-Montiel, A. Bruyant, A. Chelnokov, G. Lerondel, B. Dagens, and S. Blaize, Nano Lett. **13**, 1000 (2013).
[17]R. Blanchard, S. V. Boriskina, P. Genevet, M. A. Kats, J.-P. Tetienne, N. Yu, M. O. Scully, L. Dal Negro, and F. Capasso, Opt. Express **19**, 22113 (2011).
[18]A. Bousseksou, A. Babuty, J.-P. Tetienne, I. Moldovan-Doyen, R. Braive, G. Beaudoin, I. Sagnes, Y. De Wilde, and R. Colombelli, Opt. Express **20**, 13738 (2012).
[19]D.-S. Kim and Z. H. Kim, Opt. Express **20**, 8689 (2012).
[20]E. Yoxall, M. Navarro-Cía, M. Rahmani, S. A. Maier, and C. C. Phillips, Appl. Phys. Lett. **103**, 213110 (2013).
[21]E. C. Kinzel, J. C. Ginn, R. L. Olmon, D. J. Shelton, B. A. Lail, I. Brener, M. B. Sinclair, M. B. Raschke, and G. D. Boreman, Opt. Express **20**, 11986 (2012).
[22]J. D. Lacasse and J. Laurin, IEEE Trans. Antennas Propag. **54**, 1891 (2006).
[23]J. D'Archangel, E. Tucker, E. Kinzel, E. A. Muller, H. A. Bechtel, M. C. Martin, M. B. Raschke, and G. Boreman, Opt. Express **21**, 17150 (2013).
[24]E. Tucker, J. D. Archangel, M. Raschke, E. Briones, F. Javier Gonzalez, and G. Boreman, J. Appl. Phys. **114**, 033109 (2013).
[25]R. L. Olmon, P. M. Krenz, A. C. Jones, G. D. Boreman, and M. B. Raschke, Opt. Express **16**, 20295 (2008).
[26]F. Keilmann and R. Hillenbrand, Philos. Trans. R. Soc. London A **362**, 787 (2004).
[27]B. Knoll and F. Keilmann, Opt. Commun. **182**, 321 (2000).
[28]R. Hillenbrand and F. Keilmann, Phys. Rev. Lett. **85**, 3029 (2000).
[29]I. Horcas, R. Fernandez, J. M. Gomez-Rodriguez, J. Colchero, J. Gomez-Herrero, and A. M. Baro, Rev. Sci. Instrum. **78**, 013705 (2007).
[30]B. Deutsch, R. Hillenbrand, and L. Novotny, Opt. Express **16**, 494 (2008).
[31]F. Yang, P. Nayeri, A. Z. Elsherbeni, J. C. Ginn, D. J. Shelton, G. D. Boreman, and Y. Rahmat-Samii, IEEE Trans. Antennas Propag. **60**, 4202 (2012).
[32]J. Ginn, D. Shelton, P. Krenz, B. Lail, and G. Boreman, J. Appl. Phys. **105**, 074304 (2009).
[33]J. Huang, *Reflectarray Antenna* (John Wiley & Sons, Inc., 2005).
[34]N. Yu, P. Genevet, M. A. Kats, F. Aieta, J.-P. Tetienne, F. Capasso, and Z. Gaburro, Science **334**, 333 (2011).
[35]R. D. Javor, X.-D. Wu, and K. Chang, IEEE Trans. Antennas Propag. **43**, 932 (1995).
[36]L. A. Florence, E. C. Kinzel, R. L. Olmon, J. C. Ginn, M. B. Raschke, and G. D. Boreman, Infrared Phys. Technol. **55**, 449 (2012).
[37]D. M. Pozar, S. D. Targonski, and H. D. Syrigos, IEEE Trans. Antennas Propag. **45**, 287 (1997).
[38]A. Pors and S. I. Bozhevolnyi, Opt. Express **21**, 27438 (2013).
[39]J. C. Ginn, G. A. Ten Eyck, I. Brener, D. W. Peters, and M. B. Sinclair, "Infrared cubic dielectric resonator metamaterial," in *Photonic Metamaterials and Plasmonics, Tucson, Arizona, USA* (Optical Society of America, 2010).